Carbohydrate Polymers 164 (2017) 200–213

Contents lists available at ScienceDirect

Carbohydrate Polymers

journal homepage: www.elsevier.com/locate/carbpol

Preparation and characterization of amine functional nano-hydroxyapatite/chitosan bionanocomposite for bone tissue engineering applications

Besir Hakan Atak[a], Berna Buyuk[b], Merve Huysal[c], Sevim Isik[a,*], Mehmet Senel[d,*], Wolfgang Metzger[e], Guven Cetin[f]

[a] Department of Medical Biology, Faculty of Medicine, Fatih University, 34500, Buyukcekmece, Istanbul, Turkey
[b] Department of Chemistry, Faculty of Arts and Sciences, Fatih University, 34500, Buyukcekmece, Istanbul, Turkey
[c] Institute of Biomedical Engineering, Fatih University, B. Cekmece, Istanbul, 34500, Turkey
[d] Biotechnology Research Lab, EMC Technology Inc, ARGEM Building, Technocity, Avcılar, Istanbul, 34320, Turkey
[e] Department of Trauma, Hand and Reconstructive Surgery, Saarland University, Building 57, 66421, Homburg, Germany
[f] Division of Hematology, Department of Internal Medicine, Medical Faculty of Bezmialem Vakıf University, Turkey

ARTICLE INFO

Article history:
Received 27 April 2016
Received in revised form 29 January 2017
Accepted 31 January 2017
Available online 1 February 2017

Keywords:
Scaffold
Chitosan
Hydroxyapatite
Human mesenchymal stem cells
Osteogenic differentiation

ABSTRACT

In this study, three different types of scaffolds including a uniquely modified composite scaffold – namely chitosan (CTS), nano-hydroxyapatite/chitosan composite (CTS + nHAP), and amine group (NH_2) modified nano-hydroxyapatite/chitosan composite (CTS + nHAP-NH_2) scaffolds – were synthesized for bone tissue engineering (BTE) purposes. As results of the study, it was found that all scaffold types were biodegradable with CTS and CTS + nHAP scaffolds losing up to 15% of their initial weight, while the CTS + nHAP-NH_2 scaffold showing 10% of weight loss after six weeks of lysozyme treatment. In addition, all three types of scaffolds were shown to be biocompatible, and amongst them CTS + nHAP-NH_2 scaffolds supported the most cell proliferation in WST-1 assay and expressed the least and acceptable level of cytotoxicity in lactate dehydrogenase (LDH) test for human bone mesenchymal stem cells (hBM-MSCs). Finally, during osteoinductivity assessment, CTS + nHAP-NH_2 nearly tripled initial alkaline phosphatase (ALP) activity when whereas both CTS and CTS + nHAP scaffolds only doubled. These results indicate that all synthesized scaffold types under investigation have certain potential to be used in bone tissue engineering approaches with CTS + nHAP-NH_2 scaffold being the most promising and applicable one. In the future, we plan to intensify our studies on osteogenic differentiation on our scaffolds on a detailed molecular level and to include *in vivo* studies for pre-clinical purposes.

1. Introduction

As an alternative to autologous or allogeneic bone grafts, scaffolds made of synthetic or natural biomaterials supporting the migration, proliferation, and differentiation of allogenic bone cells might be used in bone tissue engineering (BTE). Several types of porous scaffolds have been shown to support *in vitro* bone formation by human cells, including those made of ceramics, native and synthetic polymers and composite materials (Black et al., 2015). The design of scaffolds using composite materials offers optimized patterns in terms of biodegradability and bioactivity. It is possible to materialize scaffolds with tailored physical, biological and mechanical properties by combining biopolymers and bioactive ceramics (Puppi, Federica, Piras, & Chiellini, 2010).

An ideal cellular source for BTE approaches should be non-immunogenic, non-tumorigenic, possess off-the-shelf availability,

Abbreviations: ALP, alkaline phosphatase; APTES, 3-aminopropyltriethoxysilane; BM, bone marrow; BTE, bone tissue engineering; CTS, chitosan; DMEM-LG, Dulbecco's Modified Eagle's medium low glucose; ELISA, enzyme-linked immune sorbent assay; FT-IR, Fourier transform infrared spectroscopy; hBM-MSCs, human bone mesenchymal stem cells; HMDS, hexamethyldisilazane; LDH, lactate dehydrogenase; MSC-FBS, mesenchymal Stem Cell – Qualified Fetal Bovine Serum; nHAP, nano-hydroxyapatite; PBS, phosphate buffered saline; RGD, arginylglycylaspartic acid; SEM, scanning electron microscopy; TGA, thermogravimetric analysis; WST-1, Water Soluble Tetrazolium Salt-1; XRD, X-Ray diffractometry; β-GP, β-glycerophosphate.

* Corresponding authors at: Division of Hematology, Department of Internal Medicine, Medical Faculty of Bezmialem Vakıf University, Turkey.
E-mail addresses: isiksevim@fatih.edu.tr (S. Isik), msenel81@gmail.com (M. Senel).

http://dx.doi.org/10.1016/j.carbpol.2017.01.100
0144-8617/

and potent proliferative and osteogenic potential (Gong et al., 2015; Logeart-Avramoglou, Anagnostou, Bizios, & Petite, 2005). Up to now, studies demonstrate that hBM-MSCs have the ability to differentiate into osteogenic, chondrogenic and adipogenic lineages, when incubated under appropriate *in vitro* or *in vivo* conditions (Kemp, Hows, & Donaldson, 2005; Zigdon-Giladi, Rudich, Geller, & Evron, 2015).

A scaffold for the purpose of BTE should have microstructure with interconnected and dispersed pores throughout almost its entire volume supporting cellular ingrowth and sufficient supply. Furthermore, it should exhibit sufficient mechanical stability for bearing loads after implanation. Finally, an ideal scaffold should support the formation of new bone matrix by the cells (Bessa, Casal, & Reis, 2008; Neman, Hambrecht, Cadry, & Jandialü, 2012; Sundelacruz & Kaplan, 2009). Numerous different natural materials have been studied as scaffold preparation materials and evaluated in BTE. Their biodegradability, low toxicity, renewability, and low production and disposal costs contributed the interest on natural polymers to grow in economic and environmental aspects (Shogren & Bagley, 1999). Collagen and silk fibroin are known examples of natural polymers of protein origin (Puppi et al., 2010). Hyaluronic acid, alginate, starch-based materials, bacterial cellulose, dextran and chitosan are good examples for natural polymers of polysaccharide origin (Puppi et al., 2010).

Chitosan has numerous advantages due to its properties which make it ideal as a bone graft substituent to be used in orthopedic applications (Di Martino, Sittinger, & Risbud, 2005). Chitosan is a biodegradable (Seol et al., 2004), non-toxic, biologically compatible polymer (Thano, Verhoef, & Junginger, 2001), and can be formulated in a variety of forms including powders, gels and films. In addition, it exhibits ahydrophilic surface enhancing cellular adhesion and proliferation. It was shown to promote cell growth and mineral rich matrix deposition by osteoblasts *in vitro* (Seol et al., 2004). It is highly biocompatible and inducing minimal host response due to its low immunogenity. Also, it is shown to have antibacterial activity (Ding, Deng, Du, Shi, & Wang, 2014; Younes & Rinaudo, 2015). All these reasons make CTS one of the most preferred natural polymers for BTE.

Chitosan scaffolds are flexible and their mechanical properties are weaker than those of normal bone, as it is prone to load bearing bone implants. Chitosan scaffolds alone cannot imitate all the properties of natural bone. Its mechanical weakness and instability can easily be overcome by modifications and/or use of composite structures (Di Martino et al., 2005). The development of composite materials with CTS is shown to mimic almost all supporting properties of bone tissue according to many studies in the literature (Khan & Ahmad, 2013; Rodriguez-Vazquez, Vega- Ruiz, Ramos-Zúñiga, Saldaña-Koppel, & Quiñones-Olvera, 2015). As proven, calcium phosphate materials are osteoconductive to imitate the inorganic part of a natural bone, while CTS/nHAP composite materials show promise of mimicking the organic portion as well (Teng et al., 2009; Thein-Han & Misra, 2009; Xianmiao et al., 2009).

Hydroxyapatite is a major inorganic component of the bone (Kim & Mendis, 2006). Thus, nHAP has recently emerged as an important compound for artificial bone preparation, and therefore for BTE also. It stimulates osteoconduction by a gradual replacement by the host bone after implantation. Though, the mechanical properties of nHAP are poor because of its crystalline nature, so it cannot be used in aiming of load-bearing bone tissues. Polymers have been used as combining materials to improve the mechanical properties of nHAP including its compressive strength, Young's modulus, and fracture toughness (Nath, Dey, Mukhopadhyay, & Basu, 2009). In a previous work, nHAP was used with CTS to be able to obtain a scaffold and the resulting bio-polymer composite was showed a good results and thought to be a good imitation of a functional natural bone (Sun & Yang, 2015).

In this work, we prepared a novel CTS/nHAP composite scaffold that is composed from the amine functionalized nHAP to be able to increase cell attachment. The aim of our study was to produce a unique and efficient composite scaffold to be used in BTE applications, and to biologically evaluate the pre-clinical suitability of this novel product by indicating osteoinductive and osteocunductive properties as an assessment of osteogenic differentiation success of hBM-MSCs *in vitro*.

2. Experimental part

2.1. Materials and methods

Chitosan powder (low molecular weight, 75–85% deacetylated) was purchased from Sigma–Aldrich. Calcium nitrate tetrahydrate [$Ca(NO_3)_2{\cdot}4H_2O$], 2,4,6Trinitrobenzenesulfonic acid (TNBS), diammonium hydrogen phosphate [$(NH_4)_2HPO_4$], and 25% ammonium hydroxide (NH_4OH) were purchased from Merck Millipore (Darmstadt, Germany), 3-aminopropyltriethoxysilane (APTES) were purchased from Sigma-Aldrich (Taufkirchen, Germany). All chemicals were of analytical grade and were used without further purification.

2.2. Synthesis of hydroxyapatite

nHAP nanoparticles were synthesized according to methods described in literature (Lin, Wu, & Chang, 2014). Briefly, 500 mL of 1 M $Ca(NO_3)_2{\cdot}4H_20$ aqueous solution was adjusted with NH_4OH to pH 10. The solution was heated to 90 °C, later then 500 mL of 0.6 M $(NH_4)_2HPO_4$ at pH 10 (adjusted with NH_4OH) was added dropwise under stirring. Solid parts were maintained in the reaction solution for 5 h at 90 °C; afterwards it was centrifuged at 10,000 rpm for 10 min and repeatedly washed with distilled water. The obtained product was dried and nHAP nanoparticles were obtained.

2.3. Synthesis of hydroxyapatite

The amine content of the amine functional hydroxyapatite nanoparticles were determined by TNBS assay according to literatüre (Bagheri-Khoulenjani, Mirzadeh, Etrati-Khosroshahi, & Shokrgozar, 2016). Briefly, exact amount of dried nano-composite microspheres (10 mg) were exposed to 1 mL 4% (w/v) NaHCO3 and 1 mL 0.5 (w/v) TNBS solution for 4 h at 40 °C. To hydrolysis the microspheres, 3 mL 6N HCl were added to each sample and stirred for 2 h at 60C. After cooling at room temperature, samples were diluted using deionized water and their absorption in 345 nm against the blank sample were measured using UV–vis spectrophotometer (Shimadzo- Japan). Blank samples were prepared using the same procedure unless the HCl solution was added to the samples before TNBS solution. As the interaction of TNBS and NH2 groups take places merely in basic pHs, adding HCl prevented this reaction. This procedure was repeated for 3 times for each sample.

2.4. Modification of hydroxyapatite

The surface of the nHAP nanoparticles modified according to literature (Goonasekera, Jack, Cooper-White, & Grondahl, 2010; Russo et al., 2014). 3-aminopropyltriethoxysilane (0.221 g) was added into an aqueous alcohol solution containing 90 mL of alcohol and 10 mL of water. The solution was stirred for 30 min and then nHAP (1.0 g) was added andwas stirred for 3 h. The pH was adjusted to 9–10 with NH_4OH, and the reaction was continued for another 3 h. After filtration with fitler paper the powder was first dried at room temperature and then cured at 130 °C to strengthen the silane coating by formation of a polysiloxane network struc-

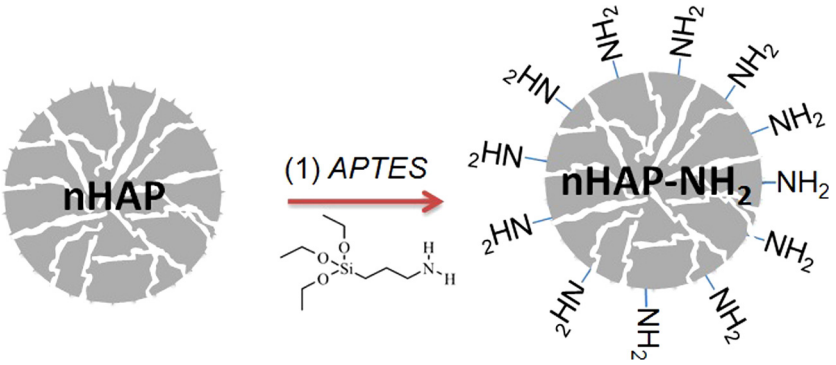

Fig. 1. Synthesis of amine functionalized modified nHAP.

ture. Hereby, the nHAP nanoparticles were modified to have NH_2 functional groups on their surfaces (Fig. 1).

2.5. Fabrication of scaffolds

As it is illustrated in Fig. 2, the scaffolds were prepared via freeze-drying method similar to the literature (Deville, Saiz, Nalla, & Tomsia, 2006; Hobbs, 1974; Luyet & Rapatz, 1958; MacKenzie, Derbyshire, & Reid, 1977; Madihally & Matthew, 1999; Zo et al., 2012). Briefly, the 2 ± 0.05% chitosan solution was prepared in 1% acetic acid with 1 ± 0.05% either NH_2-modified or unmodified HAP nanoparticles (nHAP-NH_2 or nHAP). Then, glutaraldehyde (0.25% in ddH_2O) was added to chitosan solutions and stirred for 30 min to crosslink the chitosan maxtrix. Than, the mixtures were transferred into syringe mold (Hayat Syringe 5 mL, inner diameter 1 cm, Cat. No: 8696569000227, PP), and pre-freezed shelf at −20 °C overnight in house refrigrator. Afterwards, the frozen mixtures were removed from the mold and lyophilized at −80 °C for 24 h to obtain porous scaffolds. Followingly, the lyophilized scaffolds were neutralized with 2% NaOH and 5% NaBr for 2 h, further washed with distilled water (dH_2O) and pre-freezed in the mold shelf at −20 °C overnight in house refrigrator. Finally, the scaffolds were again removed from the mold than lyophilized and stored in petri dishes shelf at −20 °C for further use.

2.6. Characterization of scaffolds

2.6.1. Porosity test

The total porosity was determined by liquid displacement method. The scaffold was immersed in a graduated cylinder containing a known volume (V_1) of ethanol. The cylinder was placed in vacuum to force the ethanol into the pores of the scaffold until no air bubbles emerged from the scaffold. The total volume of the ethanol and scaffold was then recorded as V_2. The volume difference ($V_2 - V_1$) was the volume of actual scaffold skeleton. The scaffold was then removed from ethanol and residual ethanol volume was measured as V_3. The porosity of the scaffold, was calculated using the formula below:

$$Porosity\,(\%) = \frac{V_1 - V_3}{V_2 - V_3}$$

2.6.2. Water uptake assay

Dry scaffolds were weighed (W_{dry}) and immersed in dH_2O for 24 h. Then the scaffolds were gently removed from the beaker and placed on a wire mesh rack. Excessive water was drained and scaffolds were weighed (W_{wet}) after 5 min to determine water uptake. The percentage of water absorption (E_A) of the scaffolds at equilibrium were calculated using the following formula:

$$E_A = (W_{wet} - W_{dry})/W_{dry} \times 100$$

2.6.3. Swelling test

The swelling studies were performed in phosphate buffered saline (PBS) at pH 7.4 at 37 °C. The dry weight of the scaffold was noted (W_o). Scaffolds were incubated in PBS at pH 7.4 for 7 days. Each day, the scaffolds were taken out of the PBS, and the adsorbed water on the surface was drained by filter paper. Then, the wet weight was recorded (W_w). The ratio of swelling was determined using the formula:

$$Swellingratio(\%) = [(W_w - W_o)/W_o] \times 100$$

2.6.4. In vitro degradation of scaffolds

The synthesized scaffolds were tested by using lysozyme (Sigma–Aldrich, Taufkirchen, Germany) for biodegradability. In this assay, the scaffolds were soaked in 500 μg/ml lysozyme in PBS w/o Ca^{2+}, Mg^{2+} (Biochrom GmbH, Berlin, Germany) for 6 weeks at 37 °C. At each 3 days, the medium was refreshed and end of each period; the scaffolds were taken out and washed with distilled water. Prior to enzymatic assay, the scaffold samples were weighed and the value was recorded as initial mass (W_i). At the end of each week, scaffold samples were rinsed with ddH_2O and then lyophilized to remove the water. After lyophilization, scaffolds were weighed again, and this value was recorded as final mass (W_f). The weight loss was calculated according to the formula below:

$$PercentageWeightLoss(\%) = 100 - [(W_f \times 100)/W_i]$$

Each scaffold type was studied in duplicate for any given time point, and the average of the percentages from the same type of scaffold was considered as final ratio for that scaffold type.

2.7. Structural and physical characterization of samples

Structural and morphological features and thermal properties of the samples were investigated by Fourier transform infrared spectroscopy (FT-IR), X-Ray diffractometry (XRD), scanning electron microscopy (SEM) and thermo gravimetric analysis (TGA). The crystallite size and phase structures of the samples were determined from the XRD patterns (Rigaku Smart Lab, Cu-K_α radiation). Fourier transform infrared (FT-IR) spectra of samples were recorded in transmission mode with a Bruker Alpha ATR spectrometer, in the wave number range of 400–4000 cm^{-1}. The morphological features of samples were investigated by a field emission SEM (FE-SEM, FEI Quanta FEG 450) operated at 30 kV. Powder samples were

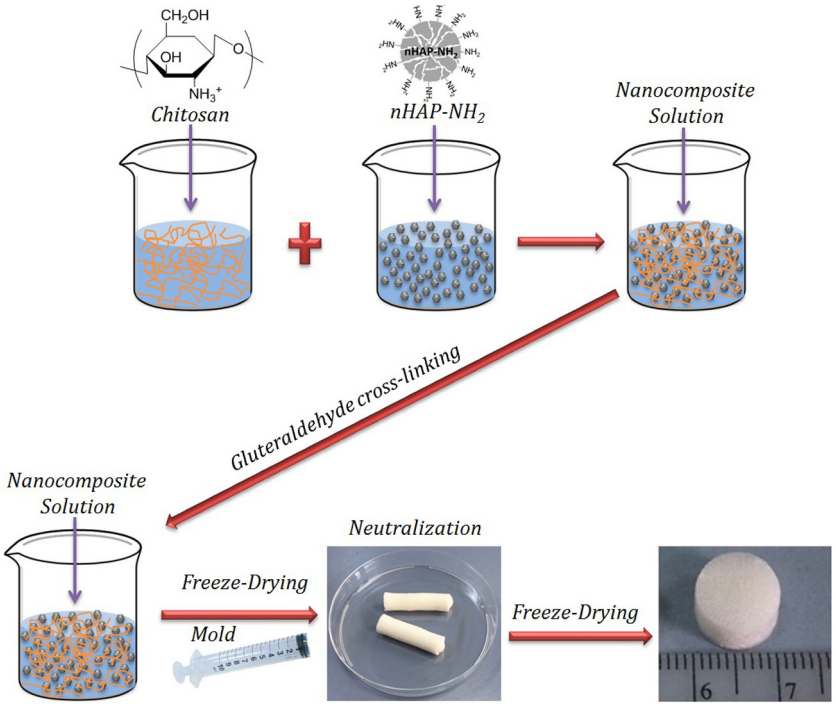

Fig. 2. Schematic illustration of the scaffold preparation.

directly imaged in the electron microscope after a proper sample preparation of sputter-coated with gold. Compression tests were performed on ten pieces of each of the sample. Compressive strength and compressive modulus values of samples were measured in a universal tensile test machine (Zwick 1446 60) in compression mode. The compressive properties of the samples were tested in the hydrated state, at room temperature. Before measurement, the samples were soaked in PBS solution at 37 °C for 24 h. The samples were subjected to axial compressive load of 2 kN kgf and with a cross-head speed of 2 mm/min. Load and displacement data were used to determine the compressive strength, relative deformation and modulus of elasticity for each sample. Five cube shaped test specimens (p = 5) with an edge-length of 5 mm were tested and the average values of mechanical parameters were reported with standart deviation. The modulus for each scaffold was calculated, using the applied load and displacement of the testing machine, together with the geometric parameters of the test samples, according to Equation (3):

$$E_s = \frac{F_R \cdot l_0}{A \cdot \Delta l}$$

where F_R is the applied load, l_0 is the initial length, A is the initial cross-sectional area, and Δl is the shortening of the scaffold during testing.

2.8. *HBM-MSC based* in vitro *biological evaluations of novel scaffolds*

2.8.1. *HBM-MSCs culture and immunophenotyping*

Bone Marrow aspirates of ten healthy volunteer donors in the age range of 18–35 were supplied from Bezmialem Vakıf University with the approval of the Ethics Committee of Fatih University, Medical School (2012.11.16, 11). Ficoll density gradient centrifuge method was used to isolate MSCs from BM using Biocoll separating solution (Biochrom GmbH, Berlin, Germany). Isolated cells were seeded in expansion medium [DMEM-LG containing 20% MSC-qualified FBS (Invitrogen, Paisley, UK), and 0.1 mg/ml Primocin (Invivogen, San Diego, CA, USA)] and incubated in an incubator under standard cell culture conditions (37 °C, 5% CO_2). Non-adherent cells were removed by medium refreshment after five days of initial seeding. Expansion medium was refreshed every three days following first medium refreshment. The hBM-MSCs in primoculture (P0) were subcultured when they reached 80–90% confluency. After each subculture, primary (P0) hBM-MSCs were denoted with increasing number of passages; P1, P2, etc.

Then, hBM-MSCs in expansion cultures were analyzed at passage 2–3 for the expression of specific surface antigens commonly used to characterize hBM-MSC populations by flow cytometry using a FACSCalibur (BD Biosciences, San Jose, CA, USA). The monoclonal antibodies were used against the human antigens CD90, CD105, CD73, CD45, CD34, and HLA-DR (BD Biosciences, San Jose, CA, USA) and their isotype controls. The positive markers – CD90, CD105, and CD73–are selected among the common mesenchymal stem cell markers presented in the literature, while the negative markers – CD45 and CD34–were members of hematopoietic surface marker family.

2.8.2. *Cell adhesion*

hMSC adhesion to the scaffolds was measured by a previously defined method utilized in similar tissue engineering studies (Pasquinelli et al., 2008). Briefly, scaffolds were placed in a 24-well plate, and pre-wetted in DMEM-LG in an incubator at least 12 h prior to cell seeding. Then, excess DMEM-LG were aspirated and hBM-MSCs (8×10^5 cells/C_{seeded}) of passage 3–5 in primary growth medium were added onto each scaffold, and cells were allowed to adhere to the scaffolds in an incubator at 37 °C, with 5% CO_2. After 4 h of incubation, cell-scaffold constructs were rinsed with PBS, and unattached cells from each scaffold were collected. Cells were counted and the cell number was denoted as C_{free}, and cell attachment success percentage on each scaffold is calculated using the formula below:

$$CellAdhesionRatio(\%) = [1 - (C_{free}/C_{seeded})] \times 100$$

Each scaffold type was studied in triplicate, and the average of the percentages from the same type of scaffold was considered as final ratio for that scaffold type.

2.8.3. Cell proliferation

Scaffolds were placed in a 96-well plate, and pre-wetted in DMEM-LG in an incubator at least 12 h prior to cell seeding. Then, hBM-MSCs (2.5×10^4 cells) of passage 3–5 in primary growth medium were seeded onto the scaffolds, and incubated for 4 h to let the seeded cells to adhere to the scaffold surfaces before completing the primary growth medium amount in each well. Cell-scaffold constructs were incubated at 37 °C, 5% CO_2 for 7 days, and cell proliferation assay was performed on days 1, 3, 5, and 7 by using WST-1 reagent (Roche Applied Science, Basel, Switzerland) according to manufacturer's instructions. Absorbances of the samples were read in an ELISA reader at 450 nm wavelength. Each scaffold type was studied in quadruplicate, and the average of the absorbance read from the same type of scaffolds was considered as final absorbance for that scaffold type.

2.8.4. Cytotoxicity Assessing/Screening

Scaffolds were placed in a 48-well plate, and pre-wetted in DMEM-LG in an incubator at least 12 h prior to cell seeding. Then, hBM-MSCs (1.0×10^5 cells) of passage 3–5 in primary growth medium were seeded onto each scaffold, and incubated for 4 h in the same fashion as it was applied for proliferative assays performed before. Cell-scaffold constructs were incubated at 37 °C, 5% CO_2 for 7 days, and toxic effect of scaffolds was analyzed on days 1, 3, 5, and 7 by using cytotoxicity detection kit (LDH) from Roche Applied Science (Basel, Switzerland) according to manufacturer's instructions. Absorbances of the samples were read in an ELISA reader at 490 nm wavelength. Each scaffold type was studied in duplicate, and the average of the absorbance read from the same type of scaffolds was considered as final absorbance for that scaffold type.

2.8.5. Visualization of hBM-MSCs by SEM

On day 3 after seeding of hBM-MSCs on CTS, CTS + nHAP and CTS + nHAP-NH_2, the DMEM-LG was removed. The samples were rinsed twice with PBS (37 °C) to remove remaining DMEM-LG. All incubations were done at room temperature under slight movement on a shaker. Attached cells were fixed with glutaraldehyde in 0.12 M aequos sodiumcacodylate buffer (pH 7.4; Sigma–Aldrich, Taufkirchen, Germany) for 10 min. The fixation solution was removed and the samples were washed three times in cacodylate buffer (0.1 M in dH_2O, pH 7.4) followed by an incubation in osmium tertroxide (1% in 0.2 M cacodylate buffer, Science Services, Munich, Germany) for 1 h in the dark. To remove remaining osmium teroxide, the samples were washed four times for 10 min in dH_2O. Before sputtering, the samples had to be dehydrated in an ascending ethanol series (three times for 10 min in 70% ethanol and once each for 10 min in 80, 90, 96 and finally 100% ethanol). Further dehydrating was done by incubation in a 1:1 mixture of 100% ethanol and hexamethyldisilazane (HMDS; Alfa Aesar, Karlsruhe, Germany) for 15 min and two additonal incubations in pure HMDS for 15 min. Finally, samples were covered with HMDS and placed under a fume hood for complete evaporation over night. The scaffolds were placed on conductive and self-adhesive carbon tabs (Plano GmbH, Wetzlar, Germany) and sputtered twice with gold-palladium (Polaron, Sputter Coater, Quorom Technologies, Ontario, Canada) and in addition once with carbon (SCD 030, Balzers Union, Balzers, Liechtenstein). A FEI XL 30 ESEM FEG (FEI, Hillsboro, OR, USA) field emission SEM was used for visualization of the cells on the scaffolds at an acceleration voltage of 5 kV in secondary electrones (SE)-mode.

2.8.6. Osteogenic differentiation

Scaffolds were placed in a 48-well plate, pre-wetted in DMEM-LG and incubated overnight prior to cell seeding. Then, hBM-MSCs (8×10^5 cells) of passage 2–4 were seeded as monolayer for positive control and onto each scaffold in osteogenic medium w/o β-Glycerophosphate [85% MesenCult MSC Basal Medium, 15% Osteogenic Stimulatory Supplement, 10^{-8} M Dex, 50 μg/ml Ascorbic acid (all from StemCell Technologies, Vancouver, BC, Canada) and 0.1 mg/ml Primocin]. Also, identical hBM-MSCs of passage 2–4 were seeded as monolayer in control medium (DMEM-LG with 15% MSC-FBS and 0.1 mg/ml Primocin) to serve as negative control during the assay. Then the scaffolds and seeded cells were incubated at 37 °C, 5% CO_2 for two weeks. After that, osteogenic medium w/β-GP (osteogenic medium with addition of 3.5 mM β-Glycerophosphate) was continued to be used for incubation period of two weeks more. During osteogenic induction, both osteogenic and control media were refreshed three times a week with corresponding media. At the end of 2nd, 3rd, and 4th weeks of incubation, control and the construct samples were rinsed with pre-warmed PBS then stored at −80 °C to be used for sample collection for ALP activity assay.

For ALP Activity Assay, scaffolds of different types were rinsed with PBS and homogenized in lysis buffer [20 mM Tris-HCl, pH 7.5, 0.3 M NaCl, 0.5% Triton-X, and 2% protease inhibitor cocktail (all from Sigma-Aldrich Taufkirchen, Germany)] with a power homogenizer (IKA, Staufen, Germany) at minimum speed for 30 s. Then, the samples were sonicated 3 times for 10 s at minimum speed with Sonopuls sonicator (Bandelin, Berlin, Germany) and incubated for 1 h at 4 °C. Finally, the samples were centrifuged at 14,000*g* at 4 °C, for 5 min and the supernatant was collected and stored at −20 °C to be used in ALP Quantification Assay.

ALP activities of differentiated hBM-MSCs on scaffolds were quantified according to manufacturer's instructions with Colorimetric Alkaline Phosphatase Assay Kit (Abcam, Cambridge, UK). Absorbance of the samples were read at 405 nm wavelength with an ELISA reader and the corresponding pNP aount was calculated using the formula obtained in the graph plotted with absorbance values of known pNP amounts in micromolars. Then, ALP enzyme activity in samples was determined according to the formula below:

$$ALPactivity(U/ml) = (A/V)/T$$

where ***A*** is amount of pNP generated by samples (in μmol), ***V*** is volume of sample added in the assay well (in ml), and ***T*** is reaction time (in minutes). Each standard and sample was measured in triplicate and the average value of the same samples were used in the calculation of ALP activity.

2.9. Statistical analysis

Statistical analysis was done with SPSS software (IBM, Armonk, NY, USA) by comparing the means among groups using the one way ANOVA test followed by Tukey's post-hoc test for individualized pairwise comparison. Significancy of the data was represented with $p \leq 0.05$. Results are presented as mean values± standard deviation.

3. Results and discussion

BTE requires scaffolds specifically designed for better healing processes. Since bone is a complex tissue and generally composed of rigid structures, characteristics of these scaffolds are highly crucial. In this study, CTS + nHAP composite scaffolds were synthesized. Then, these CTS + nHAP composite scaffolds were further modified with NH_2 groups to serve as better scaffold in many aspects for BTE purposes.

The reason for choosing nHAP as composite material arises from the fact that nHAP, whose biocompatibility and osteoinductivity

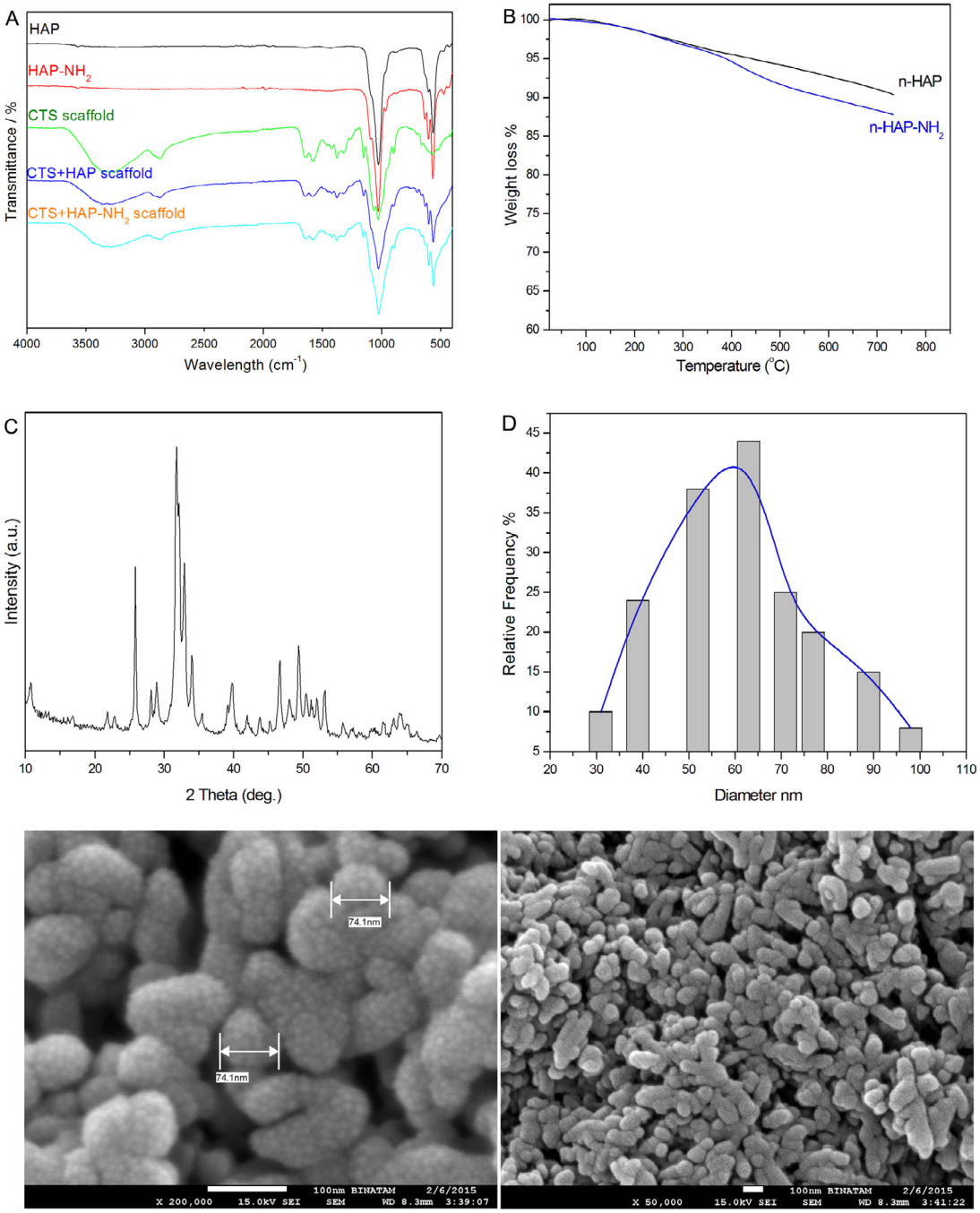

Fig. 3. (A) FTIR spectra of nHAP and nHAP-NH_2, (B) TG analysis of nHAP and nHAP-NH_2, (C) XRD pattern of nHAP and SEM images of nHAP (D) Calculated histogram from several TEM images with log-normal fitting.

are widely known, is the most abundant calcium phosphate mineral found in bones. Hwang et al. showed that microenvironments including nHAP accelerate bone formation through intramembraneous occification (Hwang, Varghese, Lee, Zhang, & Elisseeff, 2013). Additionally, Yang and colleagues found that combination of CTS with nHAP increases Ca^{2+} ions from culture medium, and thereby more nHAP crystalline growth on active surfaces, and they consolidate their findings with osteogenesis related gene expression increments as well (Yang et al., 2013).

While the effect of nHAP during bone formation is undeniable, the size and distribution of nHAP particles also cause the outcome to differ. Latterly, it was proposed that the nano-sized nHAP particles could be more effective than the micro-sized ones. In this study, nano-sized nHAP particles were homogenously dispersed over the CTS scaffolds. According to studies, nano-sized nHAP particles can trigger osteogenic pathways by higher expression levels of osteoblastic genes (Huang et al., 2012). Recently, homogenously dispersed nHAP particles on a scaffold material promoted osteogenic differentiation in a similar manner without the presence of traditional osteoinductive factors in the media (Lock, Nguyen, & Liu, 2012).

3.1. Characterization of hydroxyapatite nanoparticles

Fig. 3A shows the FT-IR spectra of nHAP, nHAP-NH_2 nanoparticles and CTS, CTS/nHAP, CTS/nHAP-NH_2 scaffolds analyses in

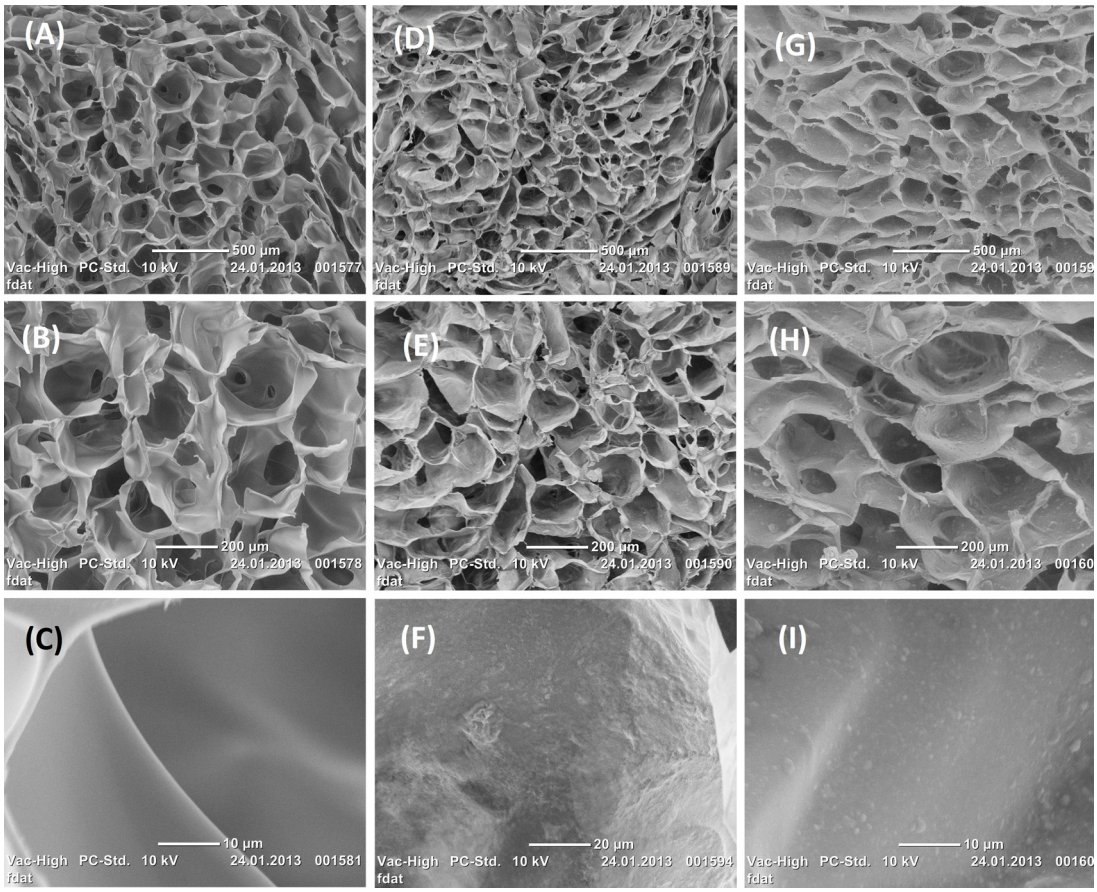

Fig. 4. SEM images of CTS (A–C), CTS + nHAP (D, E and F) and CTS + nHAP-NH_2 (G–I) scaffolds at different magnifications.

the region of 4000–400 cm^{-1}. The FT-IR analysis showed all typical absorption characteristics of hydroxyapatite. The characteristic reflections of the vibrations PO_4^{3-} at 563, 870 and 1025 cm^{-1} are observed. The stretching vibrations at 3572 cm^{-1}, vibration mode at 605 cm^{-1} are characteristic for the apatite structure due to OH^{-1} groups (Agrawal, Singh, Puri, & Prakash, 2011; Ślósarczyk et al., 2005). The functionalization of nHAP with APTES should result in coupling between surface OH groups and APTES. But this reaction can be also occurring via other moieties of the molecule. The competition situation may have caused the occurrence of the peak less (Russo et al., 2014). The number of free amine group of the nHAP-NH_2 was determined by TNBS assay and found as 2.8 µmole/g of nHAP-NH_2.

The thermal stability of nHAP and nHAP-NH_2 is shown in Fig. 3B. The thermal behavior shows a small weight loss in the temperature range from 45 to 150 °C and a continuous weight loss from 245 to 740 °C. The first stage weight loss of maximum 1% can be explained with loss of moisture. In the second degradation stage, weight decreased sharply for nHAP-NH_2 derivative by increasing of temperature with respect to nHAP. Comparing the curves, it can be seen that there was a significant difference between two types of nanoparticles which shows an evidence of NH_2 functionalization with nano nHAP (Manjubala, Scheler, Bössert, & Jandt, 2006).

The XRD diffractogram of powder sample including nHAP is shown in Fig. 3C. The XRD pattern for nHAP had many peaks in the range from about 10° to about 60° 2θ. The peaks of nHAP appearing at 26°, 30–34° and 40° (2θ) correspond to the (002), (102), (210), (211), (121), (300), (202) and (310) reflection planes. The peak at 31.7° in 2θ is assigned as a major peak of hydroxyapatite. These peak caused by (211) and (121) planes. These results are compatible with the reported nHAP (Standard JCPDS File No. 9-432) (Eslami, Hashjin, Tahriri, & Bakhshi, 2008; Hui, Meena, & Singh, 2010).

Fig. 3D shows the SEM images of nHAP nanoparticles, whose morphology was characterized by nanoparticles with sizes smaller than 80 nm in gold coated form. The average particle size for the samples was calculated as 58 ± 2 nm for the nHAP nanoparticles without gold coating using a log-normal fitting to the histograms obtained from several SEM micrographs. The SEM images show the spherical shaped particles as reported results of HAP nanoparticles (Lee, Loo, Van, Zavgorodniy, & Rohanizadeh, 2012).

3.2. Characterization of scaffolds

The FTIR spectrum of CTS scaffold (Fig. 3A) showed main bands of chitosan as follows: 3372 cm^{-1} (N—H and O—H stretching vibration), 2926 cm^{-1} (CH_3 symmetric stretch), 1581 cm^{-1} (C—N stretching vibration), 1378 cm^{-1} (CH_3 bending vibration), 1151 cm^{-1} (C—O—C bending vibration), and 1034 cm^{-1} (C—OH stretching vibration (Amin, Kandil, Awad, & Ismail, 2015). The band at 1645 cm^{-1} corresponded to imine bond (—C=N) which might be formed betweenchitosan and glutaraldehyde as well as nHAP-NH_2 and gluteraldeyhde present in the mixture. For CTS/nHAP scaffold, the characteristic absorption bands of nHAP are shown at 3372 cm^{-1} and at about 601 cm^{-1}. The broad band is related to hydroxyl group (O—H) stretching and the other band is related to P—O deformation vibrations of the PO_4^{3-} group. The bands at 2872, 1659, and 1393 cm^{-1} are due to C—H stretching, C—C stretching, C—O stretching of the CTS, respectively. Amide II band revealed at 1034 and 2863 cm^{-1}. Important interactions between CTS and HAP were clearly identified and verified using FTIR results. The

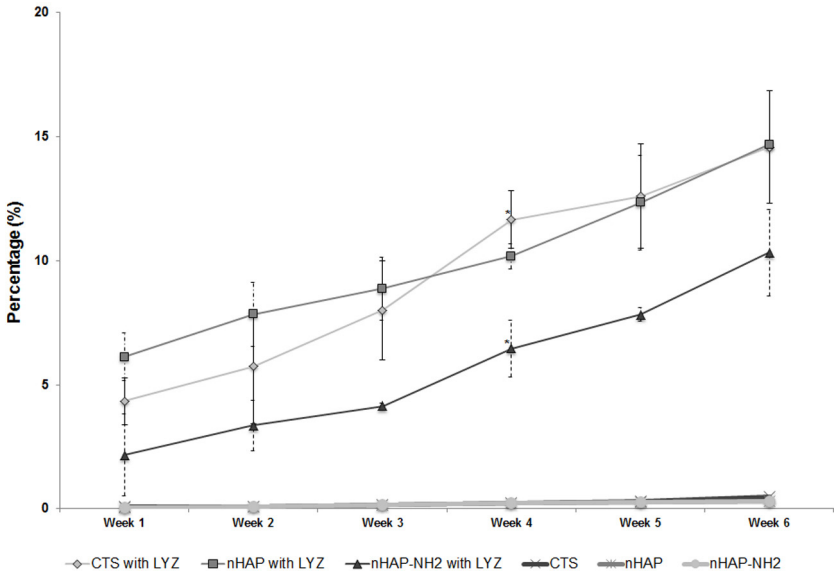

Fig. 5. Percentage weight losses of scaffolds after treatment without and with lysozyme. The assay revealed a similar – almost overlapping – degradation pattern for both CTS and CTS + nHAP scaffolds, both reaching up to 15% of total weight loss at the end of 6 weeks. Yet, the CTS + nHAP-NH_2 scaffold showed a slower degradation rate and attained 10% – approximately two-third of the other two types – of total weight loss. * represents significant weight loss with respect to CTS scaffold at that particular time point ($p < 0.05$).

band of P—O at 1024 and 601 cm^{-1} in nHAP has shifted to 1030 and 605 cm^{-1} after composite formation. (Amin et al., 2015; Fraga, de Almeida Filho, da Silva Rigo, & Boschi, 2011; Maachou et al., 2008). CS/nHAP-NH_2 composite scaffold was characterized by comparing the FTIR bands of CTS/nHAP nanocomposite scaffold. The characteristic bands for N—H appeared at 3363 cm^{-1} and as can seen it has expanded. (Shan, Qin, Chuan, Li, & Yuan, 2013).

SEM images of CTS, CTS–nHAP and CTS–nHAP-NH_2 are shown in Fig. 4. Based on the quantitative analysis of a number of micrographs according to the measurements of the JEOL JCM-5000 NeoScope SEM software (Tokyo, Japan), the pore size for CTS fabricated using 2% chitosan solution was in the range ~170–200 μm. The pore size of CTS + nHAP nanocomposite scaffolds was similar at ~140–180 μm. Similar porous structure was observed for CTS + -nHAP-NH_2 nanocomposite scaffold, implying that small variations in nHAP content did not alter the microstructure of the scaffold. The view of the scaffold indicated uniform pore structure from top to the bottom and this suggests interconnected pore pattern. As seen in Fig. 4C, the inner wall surface of CTS is smooth and, nHAP containing scaffold showed non-agglomerated distrubition of nanoparticles within chitosan matrix (Fig. 4F). The SEM images of the CTS-nHAP-NH_2 showed non-agglomerated distribution of nHAP nanoparticles within the chitosan matrix, including the pore wall (Fig. 4I). It is believed that the amine functionalized nHAP nanoparticles is helpful in the uniform distribution of nHAP-NH_2 in the scaffold matrix.

The good mechanical strength of the scaffolds is important parameter during tissue regeneration instead of adequate porosity. The effects of the nHAP and nHAP-NH_2 on the mechanical properties of the chitosan scaffolds were investigated. For this study, composite scaffolds were hydrated before mechanical analysis. As seen in Fig. S1 the incorporation of both nHAP and nHAP-NH_2 in chitosan scaffolds increased the mechanical stability of the scaffold. The significant mechanical stability of the CTS-nHAP-NH_2 scaffold possibly due to the presence of the amine functionality on the nHAP. Thus, amine functional groups of nHAP interact with chitosan via covalent crosslinking after treatment with glutaraldehyde. That might be responsible for the formation of mechanically stable scaffold structure.

Table 1
Porosity, water uptake and swelling ability of scaffolds.

Scaffold Type	Porosity [%]	Water Uptake [%]	Swelling [%]& Size (mm^3)[a]
CTS	92.5 ± 0.50	30.0 ± 1.65	29.78 ± 1.17 ~78 ± 2
CTS + nHAP	85.7 ± 3.21	20.6 ± 1.51	20.45 ± 1.26 ~69 ± 3
CTS + nHAP-NH_2	72.3 ± 4.04	18.4 ± 2.80	20.05 ± 1.46 ~67 ± 3

[a] The size of the scaffolds before swelling test was fixed to 64 mm^3 (4 × 4 × 4 mm) cubes by cutter.

3.3. Porosity of the scaffolds

Porosity is a very important factor affecting cell migration and nutrient supply in TE (Hing, 2004; Karageorgiou & Kaplan, 2005). Therefore, further characterizations of scaffolds were performed by measuring the porosity of scaffolds. The porosity of the scaffolds was measured through the liquid displacement method using ethanol. Porosity of the chitosan was 92.5 ± 0.50%. Porosity of CTS + nHAP and CTS + nHAP-NH_2 was 85.7 ± 3.21% and 72.3 ± 4.04%, respectively (Table 1). The porosity decrease in CTS-nHAP is due to the depositon of the nHAP over the scaffold matrix and the intermolecular hydrogen bonding between —NH2 groups of chitosan and —OH groups of nHAP, these result similar with previous studies Kim, Knowles, & Kim, 2004; Lan Levengood et al., 2010; Teimouri & Azadi, 2016). The porosity of the CTS-nHAP-NH_2 scaffold decreased almost up to 72%, that is the lowest among other scaffolds. This decrease probably due to the covalent crosslinking behavior of the amine functional nHAP. The scaffold porosities has decreased but still the porosity (72%) is sufficiently enough to facilitate the cell seeding and nutrient diffusion throughout the whole structure of the scaffold (Kohn, Levene, & Lhommeau, 1999). This high degree of porosity would allow cells to migrate into the scaffold and would allow for a sufficient nutrient supply.

3.4. Water uptake and swelling ability of the scaffolds

Water uptake ability of a scaffold also is another important property because scaffold might swell and damage under excess water absorption. Porosity is closely related to water uptake and

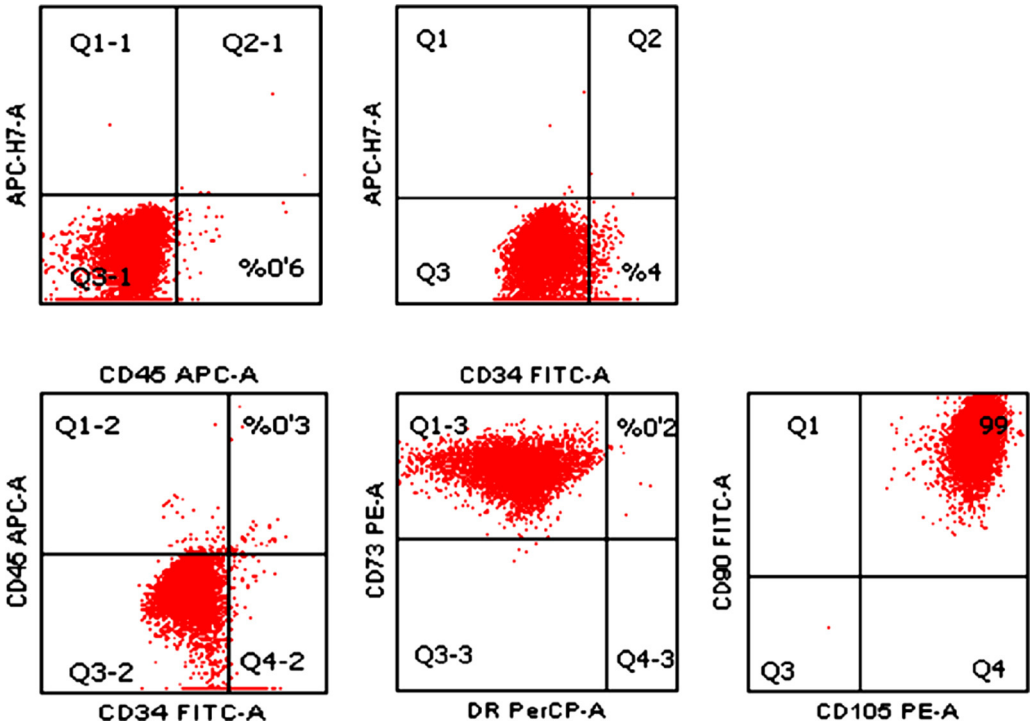

Fig. 6. Exemplary Flow Cytometry analysis. Scatter plot representation for expression of hBM-MSC surface markers. Analyzed hBM-MSCs expressed markers, CD90, CD105, and CD73 with 99.9% for all. On the other hand, they were negative for markers HLA-DR, CD45, and CD34 with 0.2%, 0.6%, and 4.0% respectively. Also, simultaneous negativity for both CD45 and CD34 markers were 0.03%.

retention properties (Chang, Huang, Yang, Kuo, & Lee, 2012). Water uptake and swelling ability of CTS was 30.0 ± 1.65% and 29.78 ± 1.17%, respectively. Water uptake and swelling ability of CTS + nHAP (20.6 ± 1.51% and 20.45 ± 1.26%) and CTS + nHAP-NH_2 was (18.4 ± 2.80% and 20.05 ± 1.46%), respectively. These results suggest that prepared scaffolds can absorb water up to 20% of their volume, and could swell to almost 20% of their size (Table 1). These results could be because nHAp formed cross-linking chains that decreased the hydrophilicity of chitosan by grafting phosphate and calcium to the hydrophilic NH_2 or OH groups. Also, the amine functional nHAP creates covalent cross-linkiing with chitosan chains. All these results showed that the scaffolds are hydrophilic which indicates that the composite scaffold can be applied potentially for tissue engineering applications because the hydrophilic nature of the scaffold will facilitate the absorption of body fluid, which consists of water mainly and is important for the diffusion of nutrient and metabolites.

3.5. In vitro *biodegradation behavior*

Biodegradability, one of the important requirements for a scaffold, provides space for tissue growth and matrix deposition. In this study, biodegradability was tested by with and without lysozyme incubation in PBS for six weeks under standard conditions. The results of the study were adequately controlled to demonstrate the relative rate of degradation between CTS, CTS + nHAP and CTS + nHAP-NH_2. There was no significant weight lost when the scaffold treated with lysozyme and this is confimed that our scaffold biodegradable with lysozyme. The activity of lysozyme does not change dramatically over time (Masuda, Ueno, & Kitabatake, 2001), nevertheless, the medium was refreshed at each 3 days. After six weeks of lysozyme treatment in PBS (0.5 mg/ml), all types of scaffolds showed continous loss of weight. However, this loss was not statistically significant throughout the assay, only in week four the CTS + nHAP-NH_2 scaffolds showed significant weight loss compared to CTS scaffold. While the CTS and CTS + nHAP scaffolds were the rapid ones in terms of degradation with up to 15% weight loss, CTS + nHAP-NH_2 scaffolds reached 10% of total weight loss, which is slower than the other two types of scaffolds (Fig. 5).

The slower degradation observed for CTS + nHAP-NH_2 scaffolds might be due to the presence of cross-linking group NH_2 within the scaffold, 10% loss of total weight is acceptable for BTE (Arvidson et al., 2011; Venkatesan & Kim, 2010). At the same time, this relatively slower degradation of CTS + nHAP-NH_2 scaffolds may indicate its structural endurance against the other types. This endurance could point out its superiority in load-bearing capability that is one of the major expectations from such BTE material (Ricciardi & Bostrom, 2013). Also, this slower degradation pattern of modified CTS + nHAP-NH_2 scaffold indicates that NH_2 groups could be used to tailor the composite scaffold in the desired way.

3.6. *Immunophenotypic characterization of hBM-MSCs*

The surface marker expressions of hBM-MSCs at passage three were identified by flow cytometry analysis. It was shown that CD90, CD105, and CD73 were highly expressed in MSCs while CD34 and CD45 were not expressed. As a result, hBM-MSCs expressed all mesenchymal lineage markers, but did not express any hematopoietic stem cell markers as expected (Fig. 6).

3.7. *Morphology and distribution of hBM-MSCs grown on scaffolds*

In recent years, designing of precise microenvironment and control of its properties has got a lot of attentions. That is important to enable in vitro studies on tissue development, disease modeling, and drug screening studies. The surface morphology and functionality are key points for the scaffold architecture due to cell

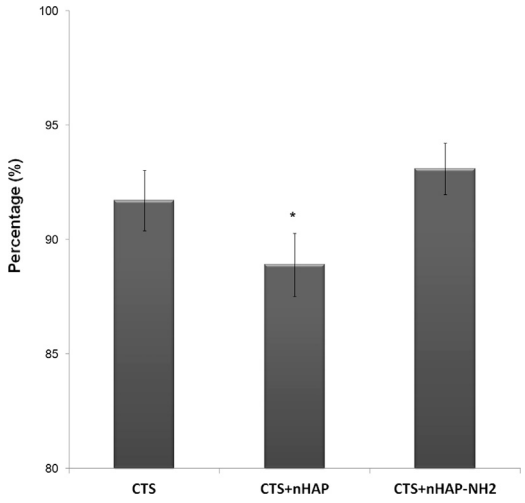

Fig. 7. Percentage of hBM-MSC attachment on scaffolds. CTS and CTS + nHAP-NH_2 scaffolds showed better cell attachment capabilities, with 91.7% and 93.1% ratios respectively, while CTS + nHAP scaffolds had cell attachment of 88.9%. * shows significancy to CTS scaffold which is served as control scaffold type ($p < 0.05$).

interactions with the surface of the host scaffold matrix. Previous studies on the effect of the surface functionality of the scaffold on the cell adhesion and behavior showed that presence of the amine group (-NH_2) beneficially influenced focal cell adhesion and cell morphology,supporting the largest cell contact area among other functional groups (Faucheux, Schweiss, Lutxzow, Werner, & Groth, 2004; Kuddannaya, Bao, & Zhang, 2015; Keselowsky, Collard, & Garcia, 2004; Keselowsky, Collard, & Garcia, 2005). Our results showed that CTS and CTS + nHAP-NH_2 scaffolds showed better cell attachment capabilities after four hours cell seeding, with 91.7% and 93.1% ratios respectively, while CTS + nHAP scaffolds had cell attachment of 88.9% (Fig. 7). According to Tukey's test, the attachment ratio of CTS + nHAP scaffold was significantly lower than the other two. These results demostrated that the CTS + nHAP-NH_2 scaffolds have best attachment success with respect to CTS and CTS + nHAP scaffolds. When nHAP was used to prepare scaffolds that was decrease the cell attachment due to itshyrdoxyl surface functionality (—OH). That is due to the amine surface functionality of the nHAP promote cell adhesion and behavior in the scaffold matix.

hBM-MSC attachment assay indicated that the cell attachment ratio on CTS + nHAP scaffolds were lower than that of CTS scaffolds ratios, mainly due to nHAP particle clumping, and physical prevention of hydrophilic attraction between CTS molecules that could accommodate attaching cells. It was reported that, cell attachment capability is one of the most crucial factors contributing a better scaffold structure since bone tissue highly relies on ECM synthesized by its cells (Neman et al., 2012). Actually, this importance should be emphasized in treatment strategies basing on autologous cells, such as hBM-MSCs, which are poor in number and generally more laborious to harvest. This unexpected outcome of composite CTS + nHAP scaffolds brought out a need for modification in purpose of improving cell attachment ratio and visually more uniform structure to aid in better BTE scaffold production. It was demonstrated that, many crosslinking agents or peptides could be used to increase cell attachment onto a scaffold (Yang et al., 2013). In this context, the RGD-binding sequence, which could be found in many ECM-molecules, is of special interest, because it is recognized by cellular integrins. Qu et al. showed that CTS + nHAP scaffolds including immobilized RGD peptides had significantly higher hBM-MSC attachment ratios with respect to CTS + nHAP scaffolds without the particular peptide (Qu, Yan j. Li, Zhuang, & Huang, 2010). So, our hypothesis was to use amine functional nHAP nanoparticles for construction of nanocomposite scaffold. The amine functionality of the nHAP gives it crosslinlink ability in the polymer matrix and also as seen in SEM images of the scaffolds the distrubition behavior also increased. Our results showed that the using NH_2 functionlized nHAP nanoparticles in the scaffold structure is a novel and applicable way in material production in BTE for a better cell attachment.

The quantitative analysis of attached cells is impressively confirmed by the exemplary chosen SEM-images shown in Fig. 8. The hBM-MSCs adhered to CTS are well-spread exhibiting a flat cell morphology. The cells formed many filopodia which are responsible for sensing the cellular environment. These typical morphological features are typical for well adhered cells (Boyan et al., 2001), which are in close contact with the surface indicating a very strong cell-surface interaction. No ablation of the cells as artefacts resulting from the preparation of the cells for SEM-imaging are visible (Fig. 8A–C). On CTS-nHAP, hBM-MSCs had problems to adhere tightly to the surface, which can be clearly seen by the unusual cell morphpolgy in Fig. 8 D, E, F. Compared to hBM-MSCs cultivated on CTS and on CTS + nHAP-NH_2, only very few and very short filopodia can be seen (Fig. 8F). The reason for the detected difference in cell adherence and cell morphology might be due to differences in surface topography or due to differences in surface chemistry. Both parameters are known to strongly influence cellular adherence (Hayes & Richards, 2010). Furthermore, the reaction of cells on the contact with an artificial surface strongly depends on the cell type used in vitro studies. Previously we were able to show, that the number of attached osteoblasts was not affected by increasing surface roughness (Metzger et al., 2014). In contrast, fibroblasts are very sensitive to an increasing surface roughness (Veith et al., 2010). Of interest, hBM-MSCs adhered well to CTS-nHAP-NH_2 exhibiting spindle shaped, but again tightly adhered cells (Fig. 8G–I). As already described for CTS, the cells are in close contact with the surface with flattened regions and numerous well-formed filopodia (Fig. 8I). These results are similar to the cell attachment results, and comfimed that the amine surface funcitoanlization of the nHAP increase the cell adhesion in the scaffold.

3.8. Viability and proliferation of hBM-MSCs on scaffolds

Biocompatibility of a scaffold material is one of the most influencing factors for its applications. In this study, proliferation assay (WST-1) and cytotoxicity assay (LDH) were performed to indicate biocompatibility of synthesized scaffolds for seven days of incubation with two-day intervals.

According to WST-1 results, hBM-MSCs on all types of scaffolds and also on tissue culture plates showed proliferation at the end of seven-day long incubation. In days 1 and 3, the scaffold groups did not show any significant difference with one other. Starting from day 5, there was a significant difference among the groups ($p < 0.05$). In the same day, Tukey's test also showed significant difference particularly between CTS and CTS + nHAP scaffolds. On day 7, all three scaffold types differed significantly ($p < 0.01$). Among the scaffolds, CTS + nHAP-NH_2 scaffold type had the most proliferative effect throughout the incubation in terms of both relative fold, and relative percentage; the cells on CTS + nHAP-NH_2 had 30% total population doubling. Though CTS + nHAP type scaffolds showed a non-proliferative state during the incubation, initially seeded cell number were reached at the end of seven-day long incubation (Fig. 9).

In the interpretation of the WST-1 assay, we did not correlate the data obtained from the cells seeded as monolayer to the cells seeded onto scaffolds, because the characteristics of hBM-MSCs may alter on two-dimensional and three-dimensional environment (Monaco, Bionaz, Hollister, & Wheeler, 2011). When the data attained from a scaffold is proportioned to its particular initial data measured on day-1, correlated outcome was demonstrated. As a

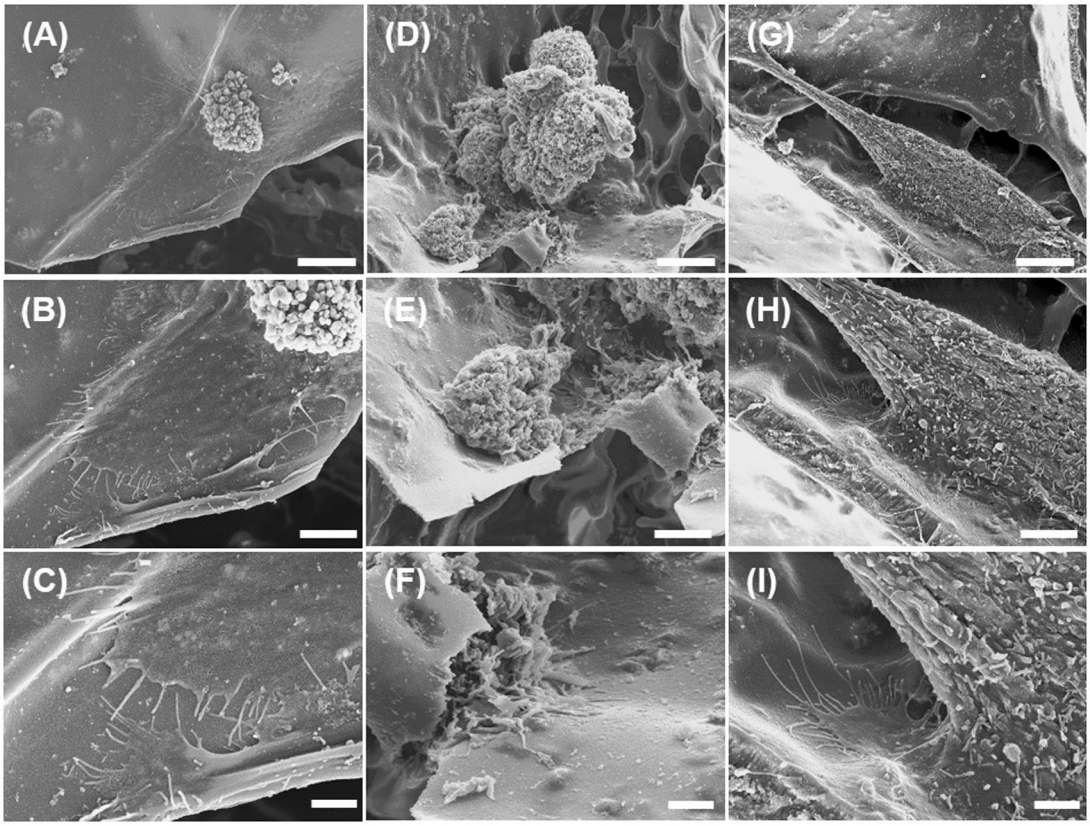

Fig. 8. Representative SEM-images of hBM-MSCs adhered to CTS (A–C), CTS + nHAP (D–F) and CTS + nHAP-NH_2 scaffolds (G–I) three days after seeding. On CTS, hBM-MSCs were well adhered, formed many filopodia and exhibited a flat and well-spread morphology, but on CTS + nHAP the cells exhibited an unsual morphology with only few and short filopodia. On CTS + nHAP-NH_2, hBM-MSCs showed a spindle-shaped morphology with some flattened areas serving as a basis for many filopodia. Scale bars 10 μm in A, D and G; 5 μm in B, E and H; 2 μm in C, F and I.

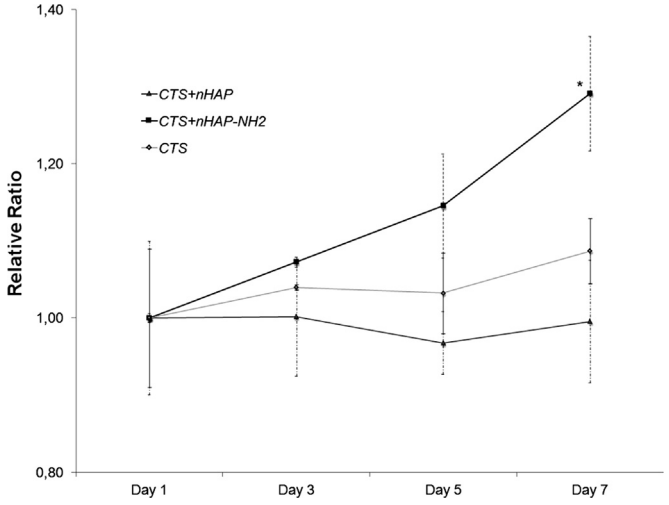

Fig. 9. Relative proliferation of hBM-MSCs on scaffolds, data normalized to Day-1 value of each particular scaffold. The cells attached onto CTS and CTS + nHAP-NH_2 scaffolds showed respectively almost 10% and 30% total population doubling over the assay period. Other than that, initially lower cell attachment ratio on CTS + nHAP scaffold eventually caused less proliferation than present on the other ones. In fact, total cell number on this scaffold type decreased after third day until fifth day, but increased again until seventh day, and almost reached its initial number at the end. * shows significancy to CTS control scaffold value of that particuar time point ($p < 0.05$).

result, CTS + nHAP-NH_2 scaffold supported constant cell proliferation, and had the most proliferative influence among the three scaffold types. The proliferative effect of chitosan composites was previously also demonstrated in several studies (Jain, Mohanty, Ray, Malhotra, & Airan, 2015; Kim et al., 2013; Zo et al., 2012), and according to our data the novel modification of nHAP particles in this study were further successful to supplemented the proliferation rate of the hBM-MSCs. Also, the results obtained in our study was in complementary to the ones from the literature (Kim et al., 2013; Zo et al., 2012)

Cytotoxic effects of scaffolds on hBM-MSCs were assayed with Cytotoxicity Detection (LDH) Plus Kit from Roche during seven days of incubation. As a result, toxicity levels of CTS + nHAP-NH_2 scaffolds were almost 5%, when CTS and CTS + nHAP type scaffolds showed relatively higher toxicities of 18% and 13% respectively (Fig. 10). CTS + nHAP-NH_2 scaffolds were contiously significantly different than CTS scaffolds throughout the assay according to Tukey's post-hoc statistical analysis, and there were a significant difference among the groups in each time point according to ANOVA. The assay shows an increasing toxicity ratio for cell-scaffold constructs. Here, waste products and dead cell accumulation, and additionally the particles and crystals of scaffold structures that are solubilized and mixed into growth media could be the reasons for this toxicity since there is not a dynamic flow of fluids in the experimental system. Although cytotoxicity levels reaching up to 18% seem high and worrisome for scaffolds' biocompatibility, this can easily be eliminated by simply refreshing the growth media in a static culture condition as ours. Moreover, WST-1 results showing constant proliferation for both scaffolds and tissue culture plate seeded control cells fortified this hypothesis. Moreover, various studies have already shown the non-cytotoxic character of chitosan-hydroxyapatite composites for tissue engineering purposes (Oliveira et al., 2006; Wang et al., 2011).

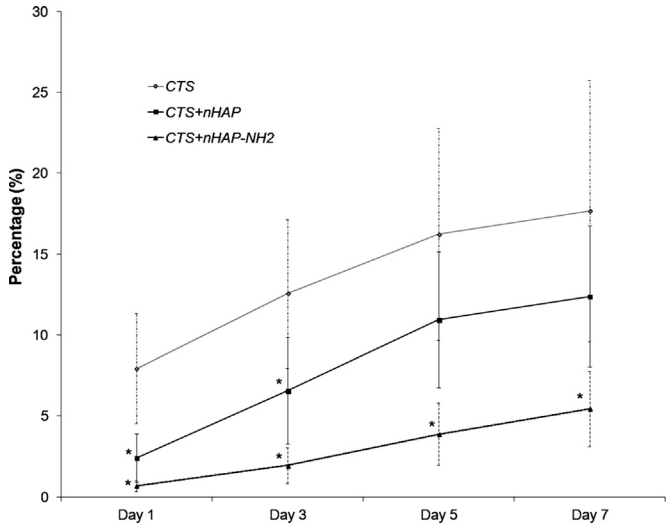

Fig. 10. Non-cumulative percentage toxicity of hBM-MSCs on scaffolds, data normalized to simultaneous WST-1 proliferation ratios. CTS scaffold showed an increasing toxicity ratio over 15% at day seven, while CTS + nHAP had toxicity of 10% at the same day. However, CTS + nHAP-NH_2 scaffold revealed very little toxicity of up to 5% for seven days of incubation, which is less than half of the toxicities of both other type of scaffolds. * shows significancy to CTS control scaffold value of that particuar time point ($p < 0.05$).

3.9. Osteogenic differentiation of hBM-MSCs on scaffolds

As the final step of this study, effect of scaffolds during osteogenic differentiation of the hBM-MSCs was investigated. Both monolayer seeded cells and scaffold seeded cells were incubated with osteogenic factors for thirty days. ALP activity which is widely used as one of the major osteogenesis assay was performed in order to evaluate the osteogenic differentiation success of hBM-MSCs on scaffold constructs (Hoemann, El-Gabalawy, & McKee, 2009). The resulted ALP amount of each control and scaffold construct was proportioned to the tenth-day amount of that particular sample to indicate fold change in total ALP amount. By presenting the ALP amount as fold change, the behavioral differences of mesenchymal stem cells in two dimensional monolayer condition and three dimensional scaffold constructs were eliminated during evaluation of assay results.

Many studies in the literature propose that mesenchymal stem cells act differently in three dimensional culture conditions than they do when cultivated as monolayer, i.e two dimensionally (Hoch & Leach, 2014). This behavioral change requires a certain amount of time for cells to adapt to a three dimensional environment after sustained two dimensional culture and adjust their cellular mechanisms accordingly. Here, the ALP activity showed that at first the cell-scaffold constructs fell short in responding the differentiation initiating factors when compared to the hBM-MSCs seeded as monolayer, i.e positive control group in the day 20. However, this impeded rate of cell-scaffold constructs during osteogenic differentiation was quickly recovered and even surpassed the differentiation rate of monolayer control groups. This would be a result of a cellular adaptation period as mentioned in the similar studies throughout the literature (Hoch & Leach, 2014; Jung et al., 2014). When we compare the effect of the scaffold types on the induction of osteogenic differentiation at day 30, CTS + nHAP-NH_2 scaffolds promoted ALP activity increase three times which is significant to all other samples including other scaffolds and control groups, while the other scaffold types led up to two times of increment in the ALP activity which is again statistically significant compared to both, negative and positive controls (Fig. 11).

4. Conclusion

In the present study, we have successfully fabricated uniquely modified composite scaffolds – namely CTS, CTS + nHAP, and CTS + nHAP-NH_2 – and characterized them for a possible use in BTE approaches. We analyzed the effects of nanocomposite scaffolds on cell attachment, survival and proliferation of hBM-MSCs as well as osteogenic differentiation compared with each other. The results demonstrated that CTS + nHAP-NH_2 scaffold was an effective surface for improved call attachment, survival and osteogenic differentiation of hBM-MSCs with respect to CTS and CTS + nHAP scaffolds. However, it is still evident that in order to achieve more conclusive results, further molecular studies including qRT-PCR of osteogenic markers (such as Osteopontin, Osteocalcin, Collagen 1, Bone Sialoprotein2, RUNX2, and CBFA1) indicating osteogenic differenetiation and also *in vivo* studies are needed.

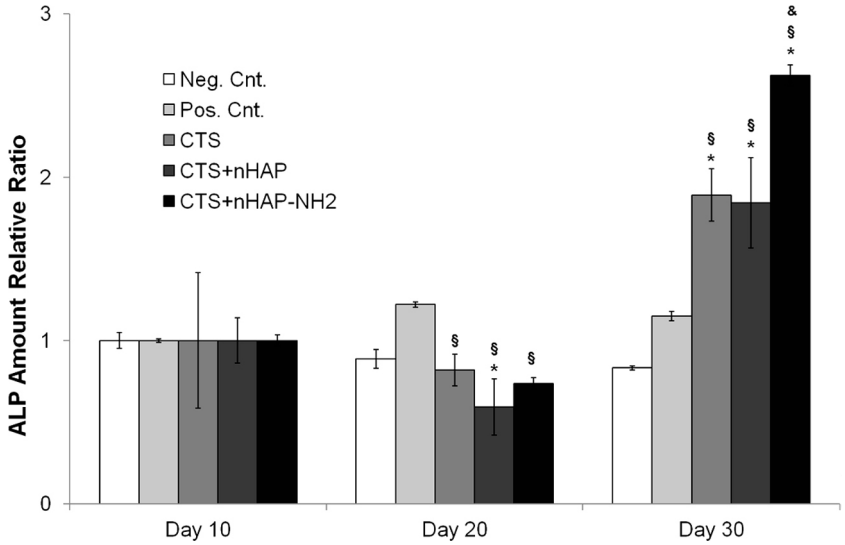

Fig. 11. ALP activity of cell free and hBM-MSC seeded scaffold. Data was normalized to ALP amount from Day-10 of each particular condition. * shows significancy to the negative control, § shows significancy to positive control, and & shows significancy to all other group values ($p < 0.05$). Better to use the introduced abbreviations.

Conflict of interest

The authors declare no competing financial interest or no conflict of interest.

Acknowledgement

This work was supported by The Scientific and Technological Research Council of Turkey, TUBITAK (Grant number: 113S009).

Appendix A. Supplementary data

Supplementary data associated with this article can be found, in the online version, at http://dx.doi.org/10.1016/j.carbpol.2017.01.100.

References

Ślósarczyk, A., Paszkiewicz, Z., & Paluszkiewicz, C. (2005). FTIR and XRD evaluation of carbonated hydroxyapatite powders synthesized by wet methods. *Journal of Molecular Structure*, *744*, 657–661.

Agrawal, K., Singh, G., Puri, D., & Prakash, S. (2011). Synthesis and characterization of hydroxyapatite powder by sol–gel method for biomedical application. *Journal of Minerals and Materials Characterization and Engineering*, *10*(8), 727–734.

Amin, A., Kandil, H., Awad, H. M., & Ismail, M. N. (2015). Preparation and characterization of chitosan–hydroxyapatite–glycopolymer/Cloisite 30 B nanocomposite for biomedical applications. *Polymer Bulletin*, *72*, 1497–1513.

Arvidson, K., Abdallah, B. M., Applegate, L. A., Baldini, N., Cenni, E., Gomez-Barrena, E., et al. (2011). Bone regeneration and stem cells. *Journal of Cellular and Molecular Medicine*, *15*(8), 718–746.

Bagheri-Khoulenjani, S., Mirzadeh, H., Etrati-Khosroshahi, M., & Shokrgozar, M. A. (2016). Development of a method for measuring and modeling the NH2 content and Crosslinking density of chitosan/gelatin/nanohydroxyapatite based microspheres. *Polymer Testing*, *51*, 20–28.

Bessa, P. C., Casal, M., & Reis, R. L. (2008). Bone morphogenetic proteins in tissue engineering: The road from laboratory to clinic, part II (BMP delivery). *Journal of Tissue Engineering and Regenerative Medicine*, *2*, 81–96.

Black, C. R., Goriainov, V., Gibbs, D., Kanczler, J., Tare, R. S., & Oreffo, R. O. (2015). Bone tissue engineering. *Current Molecular Biology Report*, *1*(3), 132–140.

Boyan, B. D., Lohmann, C. H., Dean, D. D., Sylvia, V. L., Cochran, D. L., & Schwartz, Z. (2001). Mechanisms involved in osteoblast response to implant surface morphology. *Annual Review Of Materials Research*, *31*, 357–371.

Chang, S. J., Huang, Y. T., Yang, S. C., Kuo, S. M., & Lee, M. W. (2012). In vitro properties of gellan gum sponge as the dental filling to maintain alveolar space. *Carbohydrate Polymers*, *88*(2), 684–689.

Deville, S., Saiz, E., Nalla, R. K., & Tomsia, A. P. (2006). Freezing as a path to build complex composites. *Science*, *311*(5760), 515–518.

Di Martino, A., Sittinger, M., & Risbud, M. V. (2005). Chitosan: a versatile biopolymer for orthopaedic tissue-engineering. *Biomaterials*, *26*(30), 5983–5990.

Ding, F., Deng, H., Du, Y., Shi, X., & Wang, Q. (2014). Emerging chitin and chitosan nanofibrous materials for biomedical applications. *Nanoscale*, *6*(16), 9477–9493.

Eslami, H., Hashjin, M. S., Tahriri, M. R., & Bakhshi, F. (2008). Synthesis and characterization of nanocrystalline hydroxyapatite obtained by the wet chemical technique. *Iranian Journal of Pharmaceutical Sciences*, *4*(2), 127–134.

Faucheux, N., Schweiss, R., Lutzkow, K., Werner, C., & Groth, T. (2004). Self-assembled monolayers with different terminating groups as model substrates for cell adhesion studies. *Biomaterials*, *25*, 2721–2730.

Fraga, A. F., de Almeida Filho, E., da Silva Rigo, E. C., & Boschi, A. O. (2011). Synthesis of chitosan/hydroxyapatite membranes coated with hydroxycarbonate apatite for guided tissue regeneration purposes. *Applied Surface Science*, *257*(9), 3888–3892.

Gong, T., Xie, J., Liao, J., Zhang, T., Lin, S., & Lin, Y. (2015). Nanomaterials and bone regeneration bone research. *Bone Research*, *3*, 15029.

Goonasekera, C. S., Jack, K. S., Cooper-White, J. J., & Grondahl, L. (2010). Attachment of poly(acrylic acid) to 3-aminopropyltriethoxysilane surface-modified hydroxyapatite. *Journal of Materials Chemistry B*, *1*, 5842–5852.

Hayes, J. S., & Richards, R. G. (2010). Surfaces to control tissue adhesion for osteosynthesis with metal implants: in vitro and in vivo studies to bring solutions to the patient. *Expert Review of Medical Devices*, *7*(1), 131–142.

Hing, K. A. (2004). Bone repair in the twenty-first century: biology, chemistry or engineering? *Philosophical Transactions A: Mathematical, Physical and Engineering Science*, *362*, 2821–2850.

Hobbs, P. V. (1974). *Ice physics*. New York: Oxford Univ. Press.

Hoch, A., & Leach, J. K. (2014). Concise review: Optimizing expansion of bone marrow mesenchymal stem/stromal cells for clinical applications. *Stem Cells Translational Medicine*, *3*, 643–652.

Hoemann, C. D., El-Gabalawy, H., & McKee, M. D. (2009). In vitro osteogenesis assays: influence of the primary cell source on alkaline phosphatase activity and mineralization. *Pathologie Biologie (Paris)*, *57*(4), 318–323.

Huang, Y., Zhou, G., Zheng, L., Liu, H., Niu, X., & Fan, Y. (2012). Micro-/nano- sized hydroxyapatite directs differentiation of rat bone marrow derived mesenchymal stem cells towards an osteoblast lineage. *Nanoscale*, *4*(7), 2484–2490.

Hui, P., Meena, S. L., & Singh, G. (2010). Synthesis of hydroxyapatite bio-ceramic powder by hydrothermal method. *Journal of Minerals and Materials Characterization and Engineering*, *9*(8), 683–692.

Hwang, N. S., Varghese, S., Lee, H. J., Zhang, Z., & Elisseeff, J. (2013). Biomaterials directed in vivo osteogenic differentiation of mesenchymal cells derived from human embryonic stem cells. *Tissue Engineering Part A*, *19*, 1723–1732.

Jain, K. G., Mohanty, S., Ray, A. R., Malhotra, R., & Airan, B. (2015). Culture & differentiation of mesenchymal stem cell into osteoblast on degradable biomedical composite scaffold: In vitro study. *Indian Journal of Medical Research*, *142*(6), 747–758.

Jung, O., Hanken, H., Smeets, R., Hartjen, P., Friedrich, R., Schwab, B., et al. (2014). Osteogenic differentiation of mesenchymal stem cells in fibrin-hydroxyapatite matrix in a 3-dimensional mesh scaffold. *In Vivo*, *28*, 477–482.

Karageorgiou, V., & Kaplan, D. (2005). Porosity of 3D biomaterial scaffolds and osteogenesis. *Biomaterials*, *26*(27), 5474–5491.

Kemp, K. C., Hows, J., & Donaldson, C. (2005). Bone marrow-derived mesenchymal stem cells. *Leukemia and Lymphoma*, *46*, 1531–1544.

Keselowsky, B. G., Collard, D. M., & Garcia, A. J. (2004). Surface chemistry modulates focal adhesio composition and signals through changes in integrin binding. *Biomaterials*, *25*, 5947–5954.

Keselowsky, B. G., Collard, D. M., & Garcia, A. J. (2005). Integrin binding specificity regulates biomaterial surface chemistry effects on cell differentiation. *Proceedings of the National Academy of Science*, *102*, 5953–5957.

Khan, F., & Ahmad, S. R. (2013). Polysaccharides and their derivatives for versatile tissue engineering application. *Macromolecular Bioscience*, *13*(4), 395–421.

Kim, S.-K., & Mendis, E. (2006). Bioactive compounds from marine processing byproducts – a review. *Food Research International*, *39*, 383–393.

Kim, H. W., Knowles, J. C., & Kim, H. E. (2004). Hydroxyapatite and gelatin composite foams processed via novel freeze-drying and crosslinking for use as temporary hard tissue scaffolds. *Journal of Biomedocal Materials Resarch Part A*, *72*, 136–145.

Kim, B. S., Kim, J. S., Chung, Y. S., Sin, Y. W., Ryu, K. H., Lee, J., et al. (2013). Growth and osteogenic differentiation of alveolar human bone marrow-derived mesenchymal stem cells on chitosan/hydroxyapatite composite fabric. *Journal of Biomedical Materials Research Part A*, *101*(6), 1550–1558.

Kohn, J.B., Levene, H.B., Lhommeau, C.M., (1999). Porous Polymer Scaffolds for Tissue Engineering, in Patentscope, Google Patents.

Kuddannaya, S., Bao, J., & Zhang, Y. (2015). Enhanced In vitro biocompatibility of chemically modified poly(dimethylsiloxane) surfaces for stable adhesion and long-term investigation of brain cerebral cortex cells. *ACS Applied Material Interfaces*, *7*, 25529–25538.

Lan Levengood, S. K., Polak, S. J., Wheeler, M. B., Maki, A. J., Clark, S. G., Jamison, R. D., et al. (2010). Multiscale osteointegration as a new paradigm for the design of calcium phosphate scaffolds for bone regeneration. *Biomaterials*, *31*, 3552–3563.

Lee, W. H., Loo, C. Y., Van, K. L., Zavgorodniy, A. V., & Rohanizadeh, R. (2012). Modulating protein adsorption onto hydroxyapatite particles using different amino acid treatments. *Journal of the Royal Society, Interface*, *9*, 918–927.

Lin, K., Wu, C., & Chang, J. (2014). Advances in synthesis of calcium phosphate crystals with controlled size and shape. *Acta Biomaterialia*, *10*(10), 4071–4102.

Lock, J., Nguyen, T. Y., & Liu, H. (2012). Nanophase hydroxyapatite and poly(lactide-co-glycolide) composites promote human mesenchymal stem cell adhesion and osteogenic differentiation in vitro. *Journal of Materials Science: Materials in Medicine*, *23*, 2543–2552.

Logeart-Avramoglou, D., Anagnostou, F., Bizios, R., & Petite, H. (2005). Engineering bone: challenges and obstacles. *Journal of Cellular and Molecular Medicine*, *9*(1), 72–84.

Luyet, B., & Rapatz, G. (1958). Patterns of ice formation in some aqueous solutions. *Biodynamica*, *8*(156), 1–68.

Maachou, H., Bal, K. E., Bal, Y., Chagnes, A., Cote, G., & Alliouche, D. (2008). Characterization and in vitro bioactivity of Chitosan/Hydroxyapatite composite membrane prepared by freeze-gelation method. *Trends in Biomaterials and Artificial Organs*, *22*(1), 16–27.

MacKenzie, A. P., Derbyshire, W., & Reid, D. S. (1977). Non-equilibrium freezing behaviour of aqueous systems [and discussion]. *Philosophical Transactions of the Royal Society of London B: Biological Sciences*, *278*(959), 167–189.

Madihally, S. V., & Matthew, H. W. T. (1999). Porous chitosan scaffolds for tissue engineering. *Biomaterials*, *20*(12), 1133–1142.

Manjubala, I., Scheler, S., Bössert, J., & Jandt, K. D. (2006). Mineralisation of chitosan scaffolds with nano-–-apatite formation by double diffusion technique. *Acta Biomaterialia*, *2*(1), 75–84.

Masuda, T., Ueno, Y., & Kitabatake, N. (2001). Sweetness and enzymatic activity of lysozyme. *Journal of Agricultural and Food Chemistry*, *49*(10), 4937–4941.

Metzger, W., Schwab, B., Miro, M. M., Grad, S., Simpson, A., Veith, M., et al. (2014). Induction of osteogenic differentiation by nanostructured alumina surface. *Journal of Biomedical Nanotechnology*, *10*(5), 831–845.

Monaco, E., Bionaz, M., Hollister, S. J., & Wheeler, M. B. (2011). Strategies for regeneration of the bone using porcine adult adipose-derived mesenchymal stem cells. *Theriogenology*, *75*(8), 1381–1399.

Nath, S., Dey, A., Mukhopadhyay, A., & Basu, B. (2009). Nanoindentation response of novel hydroxyapatite-mullite composites. *Materials Science and Engineering: A*, *513-514*, 197–201.
Neman, J., Hambrecht, A., Cadry, C., & Jandialü, R. (2012). Stem cell-mediated osteogenesis: therapeutic potential for bone tissue engineering. *Biologics*, *6*, 47–57.
Oliveira, J. M., Rodrigues, M. T., Silva, S. S., Malafaya, P. B., Gomes, M. E., Viegas, C. A., et al. (2006). Novel hydroxyapatite/chitosan bilayered scaffold for osteochondral tissue-engineering applications: Scaffold design and its performance when seeded with goat bone marrow stromal cells. *Biomaterials*, *27*(36), 6123–6137.
Pasquinelli, G., Orrico, C., Foroni, L., Bonafè, F., Carboni, M., Guarnieri, C., et al. (2008). Mesenchymal stem cell interaction with a non-woven hyaluronan-based scaffold suitable for tissue repair. *Journal of Anatomy*, *213*(5), 520–530.
Puppi, D., Federica, C., Piras, A. M., & Chiellini, E. (2010). Polymeric materials for bone and cartilage repair. *Journal of Progress in Polymer Science*, *35*(4), 403–440.
Qu, Z., Yan j. Li, B., Zhuang, J., & Huang, Y. (2010). Improving bone marrow stromal cell attachment on chitosan/hydroxyapatite scaffolds by an immobilized RGD peptide. *Biomedical Materials*, *5*(6), 065001.
Ricciardi, B. F., & Bostrom, M. P. (2013). Bone graft substitutes: Claims and credibility. *Seminars in Arthroplasty*, *24*, 119–123.
Rodriguez-Vazquez, M., Vega- Ruiz, B., Ramos- Zúñiga, R., Saldaña-Koppel, D. A., & Quiñones-Olvera, L. F. (2015). Chitosan and its potential use as a scaffold for tissue engineering in regenerative medicine. *BioMed Research International*, *2015*, 821279.
Russo, L., Taraballi, F., Lupo, C., Poveda, A., Jiménez-Barbero, J., Sandri, M., et al. (2014). Carbonate hydroxyapatite functionalization: a comparative study towards (bio)molecules fixation. *Interface Focus*, *4*(1), 20130040.
Seol, Y. J., Lee, J. Y., Park, Y. J., Lee, Y. M., Rhyu, Y. K. I. C., Lee, S. J., et al. (2004). Chitosan sponges as tissue engineering scaffolds for bone formation. *Biotechnology Letter*, *26*, 1037–1041.
Shan, Y., Qin, Y., Chuan, Y., Li, H., & Yuan, M. (2013). The synthesis and characterization of hydroxyapatite-β-alanine modified by grafting polymerization of γ-benzyl-L-glutamate-N-carboxyanhydride. *Molecules*, *18*(11), 13979–13991.
Shogren, R. L., & Bagley, E. B. (1999). Natural polymers as advanced materials: some research needs and directions. In *Biopolymers. Utilizing nature's advanced materials*. pp. 2–11. Cary, USA: Oxford University Press.
Sun, H., & Yang, H. L. (2015). Calcium phosphate scaffolds combined with bone morphogenetic proteins or mesenchymal stem cells in bone tissue engineering. *Chinese Medical Journal*, *128*(8), 1121–1127.
Sundelacruz, S., & Kaplan, D. L. (2009). Stem cell- and scaffold-based tissue engineering approaches to osteochondral regenerative medicine. *Seminars in Developmental Biology*, *20*(6), 646–655.
Teimouri, A., & Azadi, M. (2016). Preparation and characterization of a novel chitosan/nanodiopside/nanohydroxyapatite composite scaffolds for tissue engineering applications. *International Journal of Polymeric Materials and Polymeric Biomaterials*, *65*, 917–927.
Teng, S. H., Lee, E. J., Yoon, B. H., Shin, D. S., Kim, H. E., & Oh, J. S. (2009). Chitosan/nanohydroxyapatite composite membranes via dynamic filtration for guided bone regeneration. *Journal of Biomedical Materials Research Part A*, *88*(3), 569–580.
Thano, M., Verhoef, J. C., & Junginger, H. E. (2001). Oral drug absorption enhancement by chitosan and its derivatives. *Advanced Drug Delivery Reviews*, *52*(2), 117–126.
Thein-Han, W. W., & Misra, R. D. (2009). Biomimetic chitosan-nanohydroxyapatite composite scaffolds for bone tissue engineering. *Acta Biomaterialia*, *5*(9), 1182–1197.
Veith, M., Aktas, O. C., Metzger, W., Sossong, D., Ullah Wazir, H., Grobelsek, I., et al. (2010). Adhesion of fibroblasts on micro- and nanostructured surfaces prepared by chemical vapor deposition and pulsed laser treatment. *Biofabrication*, *2*(3), 035001.
Venkatesan, J., & Kim, S. K. (2010). Chitosan composites for bone tissue engineering-an overview. *Marine Drugs*, *8*(8), 2252–2266.
Wang, G., Zheng, L., Zhao, H., Miao, J., Sun, C., Liu, H., et al. (2011). Construction of a fluorescent nanostructured chitosan-hydroxyapatite scaffold by nanocrystallon induced biomimetic mineralization and its cell biocompatibility. *ACS Applied Material Interfaces*, *3*(5), 1692–1701.
Xianmiao, C., Yubao, L., Yi, Z., Li, Z., Jidong, L., & Huanan, W. (2009). Properties and *in vitro* biological evaluation of nano-hydroxyapatite/chitosan membranes for bone guided regeneration. *Materials Science and Engineering: C*, *29*(1), 29–35.
Yang, J., Liu, A., Han, Y., Li, Q., Tian, J., & Zhou, C. (2013). Osteo-differentiation of MSCs on chitosan/hydroxyapatite composite films? *Journal of Biomedical Materials Research Part A*, *102*(4), 1202–1209.
Younes, I., & Rinaudo, M. (2015). Chitin and chitosan preparation from marine sources. Structure, properties and applications. *Marine Drugs*, *13*(3), 1133–1174.
Zigdon-Giladi, H., Rudich, U., Geller, G. M., & Evron, A. (2015). Recent advances in bone regeneration using adult stem cells. *World Journal of Stem Cells*, *7*(3), 630–640.
Zo, S. M., Singh, D., Kumar, A., Cho, Y. W., Oh, T. H., & Han, S. S. (2012). Chitosan–hydroxyapatite macroporous matrix for bone tissue engineering. *Current Science*, *103*(12), 1438–1446.